

Active Phase Transition via Loss Engineering in a Terahertz MEMS Metamaterial

Longqing Cong, Prakash Pitchappa, Chengkuo Lee, and Ranjan Singh*

Controlling the phase of local radiation by using exotic metasurfaces has enabled promising applications in a diversified set of electromagnetic wave manipulation such as anomalous wavefront deflection, flat lenses, and holograms. Here, we theoretically and experimentally demonstrate an active phase transition in a micro-electromechanical system-based metadvice where both the phase response and the dispersion of the metamaterial cavity are dynamically tailored. The phase transition is determined by the radiative and the absorptive losses in a metal–insulator–metal cavity that obeys the coupled-mode theory. The complete understanding of the phase diagram in a reconfigurable configuration would open up avenues for designing multifunctional metadevices that can be actively switched between different phases leading to a plethora of applications in polarization control, beam deflectors, and holographic metamaterials.

Phase transitions are common phenomena in natural materials describing the transitions between solid, liquid, and gaseous states of matter. Due to the change of a certain external condition, such as temperature or pressure, structural and thermodynamical properties of the matter could change. The condition originates from the interaction between particles when thermodynamic free energy in a system is nonanalytic for some thermodynamic variables. Phase transition is also defined for nonthermodynamic systems such as dynamic phase transitions and quantum phase transitions.^[1] In quantum mechanics, parity time (PT) symmetric Hamiltonians have challenged a fundamental axiom associated with the Hermiticity of physical observables. From the pioneering observation of PT symmetry in optics,^[2] many more works have been reported extending the study into the passive systems without gain, such as in

metamaterials.^[3–5] Metamaterials are artificially constructed arrays with unit cell in the subwavelength scale that provide the flexibility to tailor the coupling and losses in the system.^[6–9] They have opened up a totally new perspective to design classical analogues in order to obtain effects and phenomena that could not be easily accessed in traditional quantum systems. One of the most exciting properties that exist in a PT symmetric Hamiltonian is the abrupt phase transition due to the spontaneous symmetry breaking across an exceptional point that is defined in a certain eigenstate space in the framework of metamaterials.^[3,10]

In addition to the phase transition in the eigenstate space, the phase transition could also be defined from the inherent optical and electrical properties of the media such as the transition from insulating state to metallic state or from amorphous state to crystalline state. The typical examples are VO₂ and GeSbTe whose states could be universally or locally manipulated for applications in memory^[11] and rewritable planar photonics devices.^[12] However, many limitations exist in the naturally occurring materials such as the extremely high/low phase transition temperature and the slow transition speed. With the design freedom of metamaterials, we could artificially engineer the physical properties at room temperature and obtain the dynamic transition through diversified stimuli such as thermal, electrostatic, magnetic, and optical pump.^[13–19] In this work, we discuss a phase transition phenomenon across a singularity in the phase diagram of a metal–insulator–metal (MIM) cavity by tailoring the loss channels in the metamaterial system. Unlike the PT symmetry breaking where the gain and loss in the system are optimized in a passive way, we control the phase of a resonant metamaterial cavity by tailoring the intrinsic radiative and nonradiative losses which are dynamically adjusted by electrostatically actuating a bimorph cantilever. Therefore, we demonstrate an active phase transition that is controlled by external voltage in a micro-electromechanical system (MEMS)-based metamaterial cavity array.

Here, we designed a metamaterial cavity design that consists of a MIM configuration as shown in **Figure 1a**. It is composed of structured metallic resonator array and a continuous metallic plane (ground plane) separated by a dielectric spacer on the substrate. The presence of the metallic ground plane prevents any transmission of light and thus only the reflected light is considered in the analysis. According to the coupled-mode theory,^[15,20,21] the reflected spectral behavior for the one-port single-mode resonator is described using the equation

L. Cong, Prof. R. Singh
Division of Physics and Applied Physics
School of Physical and Mathematical Sciences
Nanyang Technological University
Singapore 637371, Singapore
E-mail: ranjans@ntu.edu.sg

L. Cong, Prof. R. Singh
Centre for Disruptive Photonic Technologies
The Photonics Institute
School of Physical and Mathematical Sciences
Nanyang Technological University
Singapore 637371, Singapore

Dr. P. Pitchappa, Prof. C. Lee
Department of Electrical and Computer Engineering
National University of Singapore
Singapore 117576, Singapore

DOI: 10.1002/adma.201700733

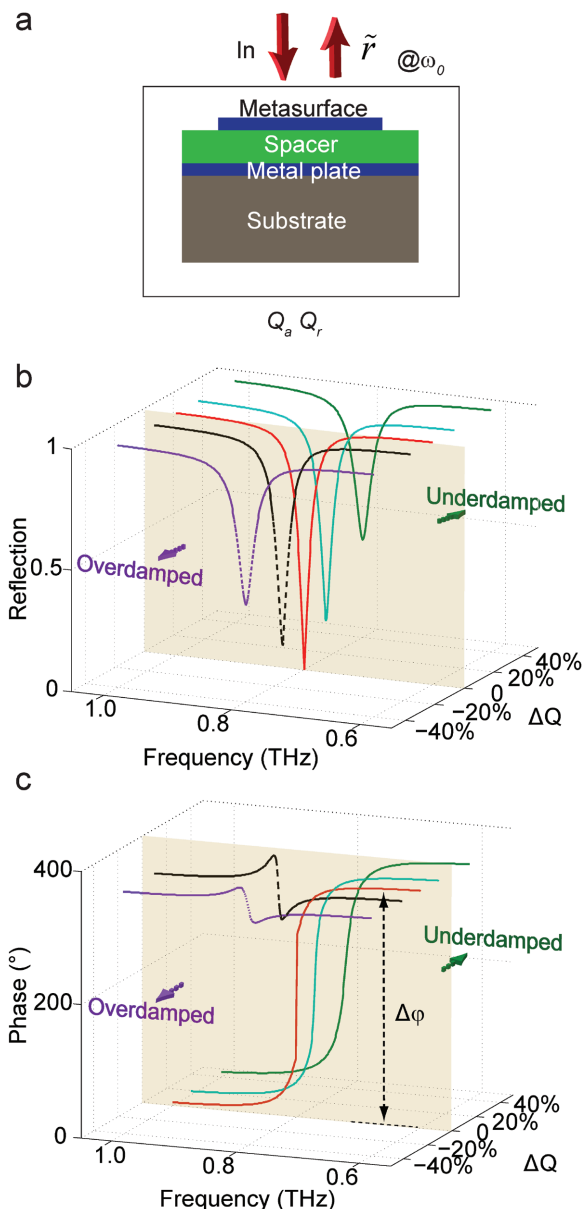


Figure 1. Model of metal–insulator–metal unit cell described by coupled-mode theory. a) Schematic of a metal–insulator–metal (MIM) unit cell in a metamaterial system described by quality factors (Q_a and Q_r) in a one-port system at resonance frequency (ω_0) that shows incident (In) and reflected (\tilde{r}) waves; b) calculated reflection amplitude and c) radiation phase spectra in the underdamped and overdamped regions using the coupled mode theory at different values of ΔQ ; $\Delta Q = (Q_a - Q_r)/(Q_a + Q_r) \times 100\%$.

$$\tilde{r} = -1 + \frac{2/\tau_r}{-i(\omega - \omega_0) + 1/\tau_a + 1/\tau_r} \quad (1)$$

where τ_a and τ_r are the lifetimes of the resonance with damping due to the intrinsic absorptive and radiative losses, respectively, and ω_0 is the resonance frequency. The quality factor of the system is defined as $Q = \omega_0\tau/2$ and thus Equation (1) can be rewritten as

$$\tilde{r} = -1 + \frac{1/Q_r}{-i(\omega/\omega_0 - 1) + 1/2Q_a + 1/2Q_r} \quad (2)$$

which indicates that the reflection spectrum is determined by the two intrinsic parameters: absorptive (nonradiative, Q_a) and radiative (Q_r) quality factors.

According to Equation (2), the amplitude and phase spectra of the cavity with five sets of (Q_a , Q_r) [(70, 30); (57.5, 42.5); (50, 50); (42.5, 57.5); (30, 70)] are calculated and presented in Figure 1b. It is well known that perfect absorption^[22] occurs at the condition of $Q_a = Q_r$, and the absorbance ($A = 1 - \text{Re}(\tilde{r})^2$) decreases significantly if any of these two quality factors deviates from the equality condition. We note that the amplitude spectra reveal identical footprints when the absolute value of ΔQ (defined as $\Delta Q = (Q_a - Q_r)/(Q_a + Q_r) \times 100\%$) is equal to each other that exhibits the symmetric behavior relative to ΔQ at the fixed resonance frequency. However, the radiation phase spectrum ($\varphi = \text{Im}(\tilde{r})$) does not possess such a symmetric behavior which reveals a stark difference between the cases of positive and negative values of ΔQ as shown in Figure 1c. The phase span ($\Delta\varphi$) is defined as the range of the reflection phase in the spectrum sweeping across the resonance frequency. We identify two operation regimes based on the value of phase span. The phase span sweeps a full 360° range in the underdamped regime ($Q_a > Q_r$, $\Delta Q > 0$) whereas it sweeps less than 180° range in the overdamped regime ($Q_a < Q_r$, $\Delta Q < 0$). Since there is no obvious signature in the amplitude spectra to differentiate the two regimes, we would mainly focus on the phase response of the reflection spectrum in order to investigate the phase diagram in different operation regimes.

The phase spectrum of the MIM system for different values of ΔQ is shown in Figure 2. First, we could clearly observe the phase transition in the phase span plot that reveals different behaviors in the underdamped and the overdamped regimes. As shown in Figure 2a, the phase span shows an obvious dependence on negative values of ΔQ in the overdamped region where the phase span variation is less than 180° . However, at $\Delta Q = 0$, we observe an abrupt phase transition in the MIM system. As ΔQ becomes positive, the operation state of the MIM cavity changes to an underdamped regime where the phase span remains constant at 360° irrespective of the value of ΔQ . The calculated raw phase spectra data retrieved from the coupled mode theory are shown as an inset in Figure 2a where we could also clearly observe the variable phase span across the resonance frequency from the overdamped to the underdamped regime. The operation of the MIM system in the underdamped region could have tremendous applications in metasurface devices with designer planar optical functionalities^[23,24] such as flat lenses,^[25,26] holographic display,^[27,28] and digitally encoded metamaterials.^[29–31] While operating in the overdamped region, the strong dependence of phase span on the value of ΔQ would provide a robust platform for phase/dispersion based sensing of the perturbations in the external environment.^[32,33] The phase transition between the two operation states enables a dynamic switching effect which could be useful in designing multifunctional reconfigurable metadevices.

For the metadevices operating in the underdamped and the overdamped regimes, the slope of the phase spectrum around resonance is also significant since it determines the stability and the accuracy of the device. Although the value of phase span is constant when the MIM cavity operates in the underdamped regime, the phase response shows different slopes

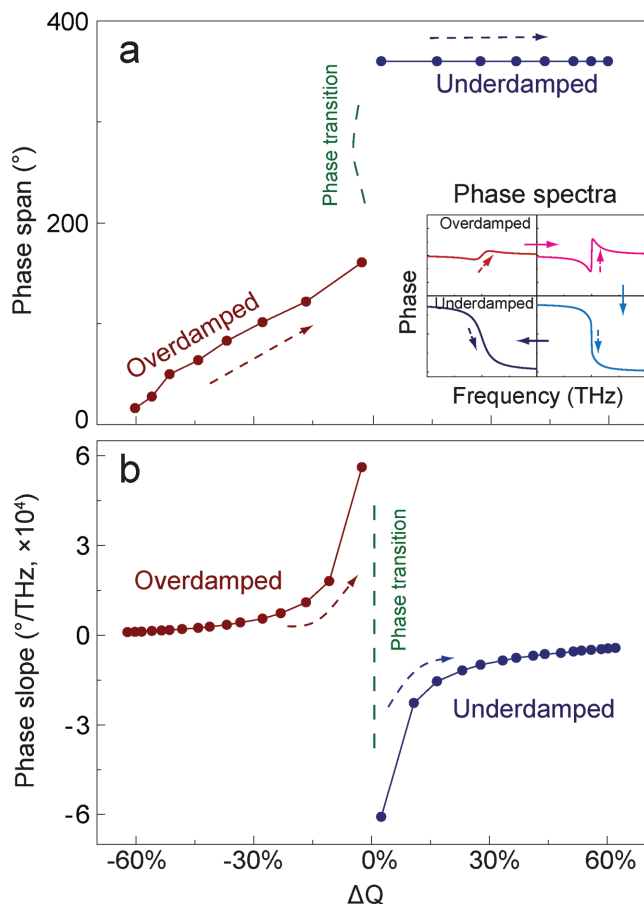


Figure 2. Phase spectral properties in the underdamped and overdamped regimes. a) The evolution of the phase-span at different values of ΔQ , the critical value of phase transition occurs at $\Delta Q = 0\%$. Inset shows the frequency-dependent phase response spectra at four different values of ΔQ , where the phase-span is less than 180° in the overdamped regime and remains constant at 360° in the underdamped regime. The phase slope at the center resonance frequency indicated by the corresponding arrows varies with the value of ΔQ . All the phase-span and phase slope values are retrieved from the calculated phase response spectra. b) The phase slope describes the dispersion at different values of ΔQ and the critical phase transition occurs at $\Delta Q = 0\%$.

($d\phi/d\omega$) at different values of ΔQ as shown by the dashed arrows in the inset of Figure 2a which indicates the tunable dispersion of the MIM cavity. In order to numerically show the dependence of the dispersion on ΔQ , we calculated the slope of the phase response spectra at the central resonance frequency (0.8 THz) as presented in Figure 2b. We observe a symmetric dependence on the value of ΔQ for the phase slope in these two operation regimes. A singularity exists in the phase slope spectrum where the slope diverges to infinite positive value in the overdamped region and infinite negative value in the underdamped region, respectively, when ΔQ approaches the critical phase transition point ($\Delta Q = 0$). The sudden phase transition leads to the opposite signs of phase slope from positive values in the overdamped region to negative values in the underdamped region. Therefore, the dispersion in the MIM cavity undergoes a phase reversal which leads to a dynamic switching caused by tailoring the difference between the radiative and the

nonradiative quality factors. In order to engineer the inequality between the two loss channels, it is essential to clarify the role of the intrinsic parameters that control the two different quality factors in the MIM system.

We resort to the mode-expansion theory (MET) in order to explain the loss parameters in the MIM resonator.^[15,34,35] Let us assume a simple subwavelength grating unit cell with period p , slot width a , metal thickness h_m , and spacer thickness h ($p \ll \lambda$, $h < \lambda$, $a \ll p$). For the radiative quality factor, it is described as the ratio of the total stored energy inside the MIM cavity $\langle U \rangle$ to the energy radiated by the cavity per time-oscillation cycle $\langle P_r \rangle$

$$Q_r = \frac{\omega_0 \langle U \rangle}{\langle P_r \rangle} = \frac{1}{2k_0 h} \sum_m \Gamma(m) \frac{\sin^2(m\pi a/p)}{(m\pi a/p)^2} \quad (3)$$

where $\Gamma(m) = \epsilon k_0^2 [(2m\pi/p)^2 + \epsilon k_0^2] / [(2m\pi/p)^2 - \epsilon k_0^2]^2$ weighs the m th order mode contribution in the MIM cavity and ϵ is the spacer permittivity. The coupling between external field and the m th order mode is described as $\sin^2(m\pi a/p) / (m\pi a/p)^2$. The total energy $\langle U \rangle$ in Equation (3) is deduced from three nonzero field components (H_y , E_x , E_z) assuming the grating to be oriented along the y -axis. The radiated energy $\langle P_r \rangle$ is calculated by $\langle P_r \rangle = 2p \sqrt{\frac{\epsilon_0}{\mu_0}} |\vec{E}_o \cdot \vec{j}|^2$ (details of the deduction can be found in the Supporting Information). Here, we ignore the ohmic losses from the metal and the spacer layer since these parameters account for the absorptive quality factor. The absorptive quality factor is defined as the ratio of total energy $\langle U \rangle$ to the time-averaged energy absorbed by the cavity that is derived as

$$Q_a = \frac{\omega_0 \langle U \rangle}{\langle P_a \rangle + \langle P_m \rangle} = \frac{\text{Re}(\epsilon) h p}{\alpha \text{Im}(\epsilon) h p + \beta (2p - a) H(\delta)} \quad (4)$$

where $\langle P_a \rangle$ and $\langle P_m \rangle$ are the absorbed energy by spacer and metal, respectively. α and β describe the relative contributions in absorption by spacer and metal layers, respectively. The effective field-decay length in metal is $H(\delta) = \delta(1 - e^{-2h_m/\delta})$ with δ being the skin depth ($\delta = \sqrt{2/\mu_0 \omega_0 \sigma_m}$). The absorption is calculated by integrating $\frac{1}{2} \text{Re}(\vec{E}^* \cdot \vec{j})$ in one unit cell (details can be found in the Supporting Information).

From Equations (3) and (4), we could analytically understand the parameters that tailor the radiative and the absorptive quality factors. In addition to the geometrical and material parameters of the resonator that determine the quality factors, the spacer thickness (h) reveals an interesting impact on the radiative and the absorptive quality factors. The radiative quality factor Q_r shows an inverse proportionality to h and Q_a is directly proportional to h by ignoring the loss contribution from the spacer due to the small loss tangent of SiO_2 . The direct and inverse proportionality of absorptive and radiative quality factors by tailoring the dielectric spacer thickness h provides a simple pathway to tune the difference between the quality factors (ΔQ). Taking advantage of the suspended bimorph cantilevers residing on top of the spacer layer in a MEMS-based metadevice, the effective spacer thickness of the MIM cavity (the addition of spacer layer thickness and effective thickness of air space between spacer layer and the out-of-plane suspended

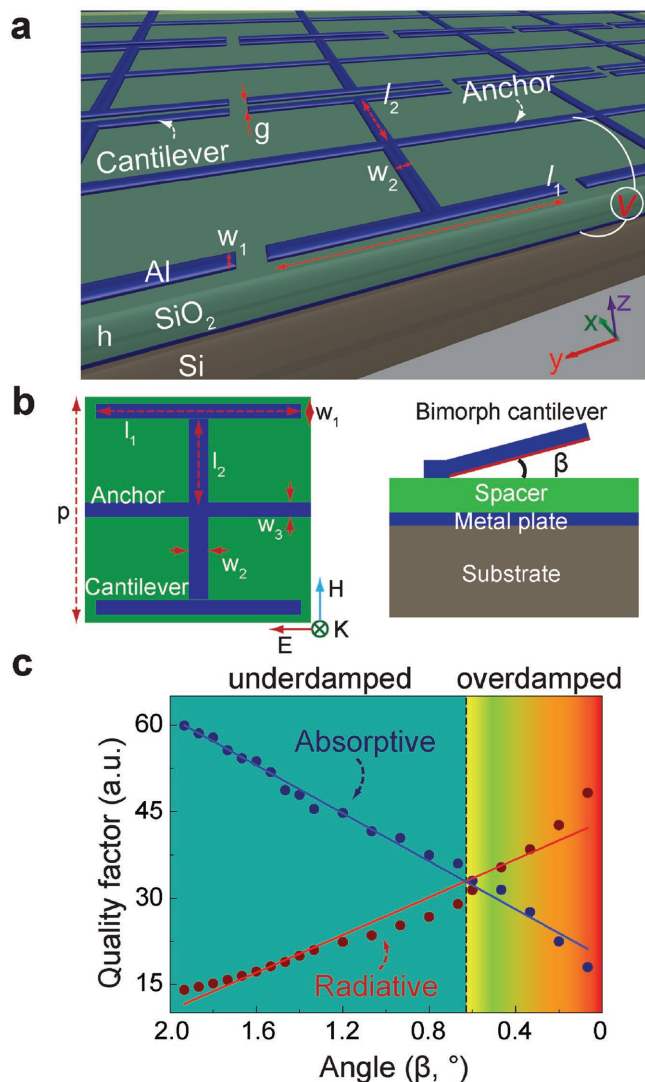


Figure 3. The schematic illustration of the MEMS-based MIM design for tailoring the radiative and the absorptive quality factors. a) The perspective illustration of the MEMS-based metamaterial design. b) Schematic top view (at “ON” state) and side view (at “OFF” state) of a unit cell in the MEMS-based MIM metamaterial array. The SiO₂ spacer thickness is $h = 5 \mu\text{m}$ and the cantilever and anchor are made of aluminum whose thickness is 500 nm . The thickness of the bottom plane aluminum reflector is $1 \mu\text{m}$. All the other geometrical parameters are presented in the image where $g = 4$, $w_1 = w_3 = 4$, $l_1 = 100$, $w_2 = 6$, and $l_2 = 50$ (in μm). The period p of the square unit cell is $104 \mu\text{m}$. c) The retrieved radiative and absorptive quality factors of the MEMS-based MIM array at different cantilever angles.

cantilever) could be actively controlled by actuating the reconfigurable cantilevers.^[13,36] A design of the structured MEMS metamaterial array with detailed parameters and top/side views of a unit cell are schematically presented in Figure 3a,b, respectively. The cantilevers are released to bend up with an initial angle after the fabrication due to the residual stress in the bimorph configuration. The bent up angle is defined as β and the initial angle is estimated to be $\approx 2^\circ$ for this specific design (depending on the length and thickness of cantilevers)^[36] which is defined as the “OFF” state (no external voltage applied). The

electrostatic voltage is applied on the anchor and bottom metal plate as illustrated in Figure 3a, which would give rise to an attractive force pulling the suspended cantilevers closer to the spacer layer. The gap between the suspended cantilevers and spacer layer vanishes at a critical voltage when the cantilever snaps down to touch the spacer layer due to the strong electrostatic attraction. This critical voltage is also known as the pull-in voltage. The angle β becomes 0° and this state is defined as the “ON” with the applied pull-in voltage. In this MEMS-based MIM metamaterial array, the active control of the suspended cantilevers (angle, β) adjusts the effective spacer thickness whose relationship is estimated as $h_{\text{eff}} = \frac{l^2 \beta \cdot n_0}{2p \cdot n_{\text{SiO}_2}} + h$ by consid-

ering the out-of-plane cantilever as a straight line with a small angle β (see the Supporting Information). Here l is the effective length of cantilever, p is the period of one unit cell, h is the thickness of SiO₂ spacer, n_0 is the refractive index of air, and n_{SiO_2} is the refractive index of SiO₂, respectively. With the linear dependence of the effective spacer thickness on the cantilever angle β , the radiative and the absorptive quality factors would be proportional to the cantilever angle β according to Equations (3) and (4).

We first performed the numerical simulations by building a model of the MIM unit cell in Figure 3b using a commercially available software Computer Simulation Technology (CST®) Microwave Studio. The simulated reflection spectra were fitted using Equation (2), and the absorptive and radiative quality factors were extracted from the fitting parameters at different angles β as shown in Figure 3c. The two quality factors exhibit the approximate linear dependence on the effective angle of cantilevers (smaller than 2°) that coincides with the theoretical prediction of MET. In addition, the inequality between the two quality factors switches at $\beta \approx 0.6^\circ$ leading to the phase transition between the underdamped and the overdamped regimes.

Based on the simulated results and the observation of phase transition using the MEMS-based metamaterial, the device was fabricated using plasma enhanced chemical vapor deposition (PECVD) and atomic layer deposition (ALD) combined with the photolithography process (see the Experimental Section for details). The sample images at the “ON” and “OFF” states are presented in Figure 4a,b, respectively. The initial state of the cantilevers in the MEMS metamaterial is “OFF” with suspended cantilevers after the release process in vapor hydrofluoric acid (VHF) that etches the sacrificial layer. The cantilevers are pulled back to touch the spacer layer (“ON” state) by applying the pull-in voltage. The intrinsic switching speed of cantilevers is estimated to be in the sub-MHz range that is limited by the first order mechanical resonance frequency of the cantilevers and also affected by the adhesion force from the interface quality between cantilevers and spacer. In repeatability tests, stiction may affect the uniformity of the array where several cantilevers would be stuck when the van der Waals force of attraction becomes larger than the spring restoring force of the microcantilevers. Degradation due to material transfer may also occur in a few of unit cells which would not have a drastic effect on the collective resonance behavior of the metamaterial array with thousands of unit cells. We are seeking for other solutions for the complex MEMS configuration with more stable and uniform response such as torsional actuators using silicon. The

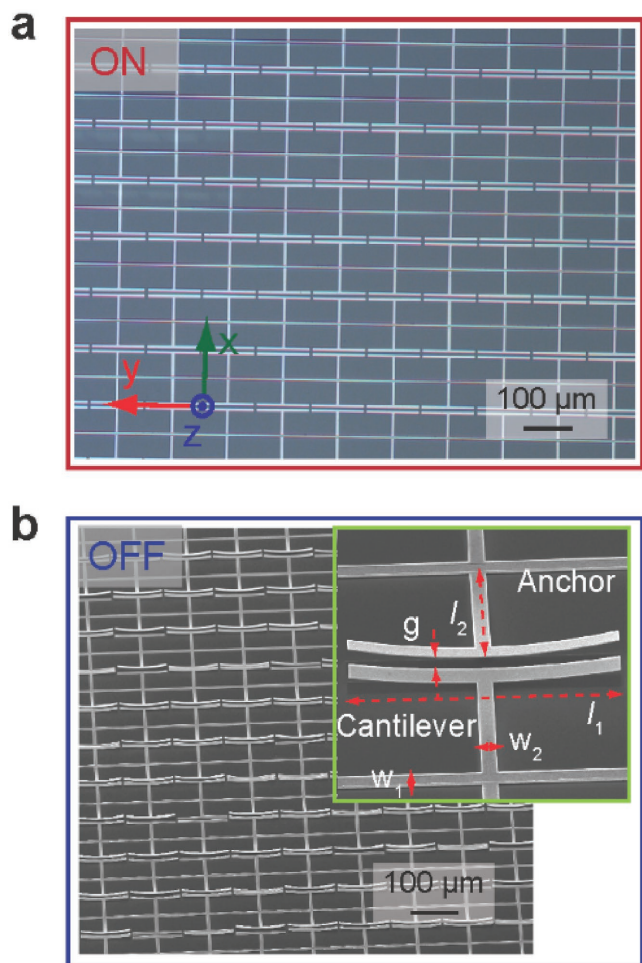


Figure 4. The images of the MEMS-based MIM samples. a) The “ON” state microscopic image of the fabricated MEMS-based metamaterial array. b) The “OFF” state scanning electron microscope image of the sample with detailed geometric parameters.

fabricated sample was designed with the identical geometrical parameters as indicated in the simulated model.

The measurements of the metadvice response in the reflection spectrum were performed using the terahertz time-domain spectroscopy system in dry air atmosphere for samples and references (a standard aluminum plate). The measured time-domain signals were Fourier transformed to the frequency-domain spectra with amplitude and phase information that is normalized to the reference signals by $\tilde{r}(\omega) = \tilde{r}_s(\omega)/\tilde{r}_r(\omega)$ where $\tilde{r}_s(\omega)$ is the reflection signal of sample and $\tilde{r}_r(\omega)$ is the reference signal, respectively. The measured amplitude and phase spectra of the MEMS metamaterial at the “ON” and “OFF” states are presented in **Figure 5a,b**. A resonance is observed at 1.34 THz which represents the “OFF” state that originates from the dipolar resonance of the suspended cantilevers for the γ -polarized incidence. The resonance redshifts to 0.74 THz in the “ON” state due to the change in the equivalent inductance and capacitance in the system determined by the effective length of cantilever and thickness of effective spacer when the cantilever is pulled down.^[37] As predicted by the analytical model and the

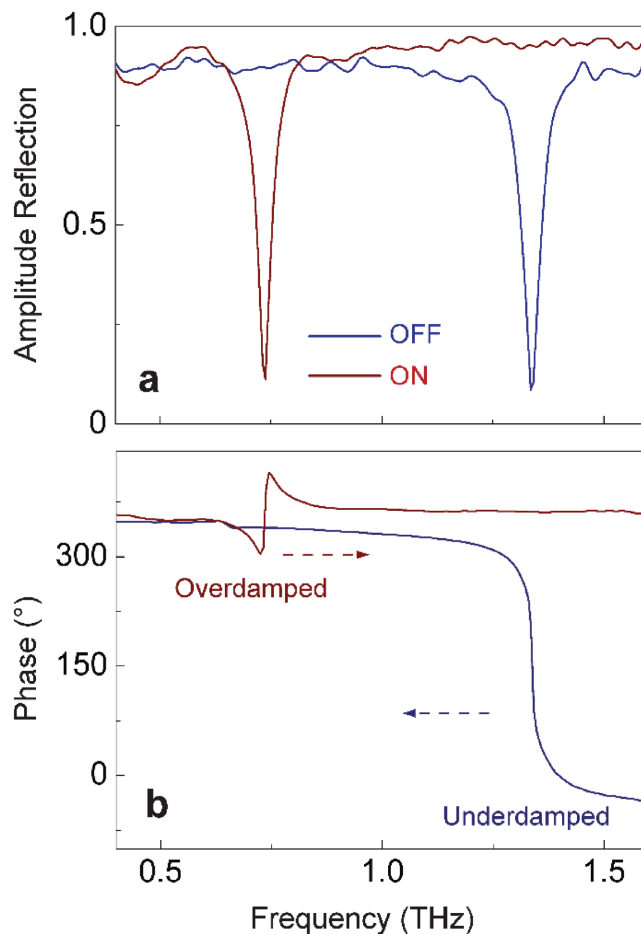


Figure 5. The measured results. a) The reflection amplitude spectra and b) the phase spectra of the MEMS-based MIM metamaterial operating in the “ON” and the “OFF” states.

numerical simulations, the inequality between the two quality factors in the system would be switched while operating in the “ON” and “OFF” states that induces the phase transition. Such a dynamic phase transition is verified by the phase spectra shown in **Figure 5b**. It is clearly observed in phase spectra that: (1) The phase span covers a full 360° range in the “OFF” state indicating the operation in underdamped regime ($\Delta Q > 0$) and it covers a less than 180° range in the “ON” state indicating the operation in an overdamped regime ($\Delta Q < 0$). (2) The phase slope is switched from negative at “OFF” state to positive at “ON” state indicating the switching effect in the intrinsic dispersion of the resonant cavity. Therefore, we have experimentally demonstrated the active phase transition of the MEMS-based metamaterial between underdamped and overdamped regimes by manipulating the radiative and absorptive losses.

In summary, we have theoretically and experimentally discussed an active phase transition in the MIM system from the aspect of phase-span and resonant dispersion using MEMS technology. The reflection spectrum is analyzed using coupled-mode theory where the inequality between radiative and absorptive quality factors determines the state of operation. The

dynamic phase transition by the electrostatic actuation of cantilevers in the MEMS-based metamaterial is interpreted from the mode-expansion theory. The complete understanding and arbitrary control of the phase response is crucial in metamaterial systems for the manipulation of the local radiation in the recently developed ultrathin metasurface based applications such as anomalous wavefront deflection, hologram, flat lenses, and polarization-based devices. With the development of more stable, uniform and accurate micro- or nanocantilevers, the combination of MEMS technology with metamaterial would hold the promise for developing the next generation multifunctional reconfigurable metadevices.

Experimental Section

Fabrication: The metadvice was fabricated using a complementary metal-oxide-semiconductor (CMOS) compatible process as described below. First, the substrate (8 in. silicon wafer) was deposited with 1 μm thick aluminum (Al) reflector layer. On top of the reflector, spacer (5 μm thick silicon oxide) was deposited using PECVD method (see the Supporting Information). Following this, a 100 nm aluminum oxide (Al_2O_3) layer was deposited using ALD process in order to prevent the etching of spacer SiO_2 during the release process. On top of this layer, a 100 nm thick SiO_2 sacrificial layer was deposited using PECVD method.

Second, conventional photolithography process was used to pattern the anchors. With the designed pattern, the parts of sacrificial SiO_2 for anchor regions were dry etched. After this, a 50 nm thick Al_2O_3 layer was deposited using the ALD process, followed by the sputter deposition process of 500 nm thick Al. Note that the bimorph layers ($\text{Al}/\text{Al}_2\text{O}_3$) were in physical contact with bottom Al_2O_3 layer at the anchor region, and in the remaining part of the wafer, it was on top of SiO_2 layer.

Third, it was moved to the step of defining the cantilevers and metal lines of metadvice patterns by another photolithography process. After this, both Al and Al_2O_3 layers were dry etched to form the designed metadvice pattern. Finally, VHF was used to isotropically etch the SiO_2 sacrificial layer away, thereby suspending the cantilevers over the spacer with an air gap between them. At the anchor region, the bimorphs were in physical contact with spacer layer; hence the VHF release process was not time controlled, and this ensured higher yield of the devices. Due to the residual stress in the bimorph cantilevers, the released cantilevers were bent up, thereby increasing the initial tip displacement that was defined as the "OFF" state.

Supporting Information

Supporting Information is available from the Wiley Online Library or from the author.

Acknowledgements

The authors acknowledge Nanyang Technological University startup Grant No. M4081282, Singapore Ministry of Education Grant Nos. M4011362, M4011534, MOE2011-T3-1-005, and MOE2015-T2-2-103 for funding of this research.

Conflict of Interest

The authors declare no conflict of interest.

Keywords

active metamaterials, loss engineering, MEMS, phase transition, terahertz

Received: February 6, 2017

Revised: March 25, 2017

Published online:

- [1] G. Jaeger, *Arch. Hist. Exact Sci.* **1998**, *53*, 51.
- [2] C. E. Rüter, K. G. Makris, R. El-Ganainy, D. N. Christodoulides, M. Segev, D. Kip, *Nat. Phys.* **2010**, *6*, 192.
- [3] M. Lawrence, N. Xu, X. Zhang, L. Cong, J. Han, W. Zhang, S. Zhang, *Phys. Rev. Lett.* **2014**, *113*, 093901.
- [4] A. Guo, G. Salamo, D. Duchesne, R. Morandotti, M. Volatier-Ravat, V. Aimez, G. Siviloglou, D. Christodoulides, *Phys. Rev. Lett.* **2009**, *103*, 093902.
- [5] M. Kang, F. Liu, J. Li, *Phys. Rev. A* **2013**, *87*, 053824.
- [6] D. R. Smith, J. B. Pendry, M. C. Wiltshire, *Science* **2004**, *305*, 788.
- [7] L. Cong, Y. K. Srivastava, R. Singh, *Appl. Phys. Lett.* **2016**, *108*, 011110.
- [8] R. Singh, I. Al-Naib, D. R. Chowdhury, L. Cong, C. Rockstuhl, W. Zhang, *Appl. Phys. Lett.* **2014**, *105*, 081108.
- [9] L. Cong, N. Xu, J. Han, W. Zhang, R. Singh, *Adv. Mater.* **2015**, *27*, 6630.
- [10] M. Kang, J. Chen, Y. Chong, *Phys. Rev. A* **2016**, *94*, 033834.
- [11] T. Driscoll, H. T. Kim, B. G. Chae, B. J. Kim, Y. W. Lee, N. M. Jokerst, S. Palit, D. R. Smith, M. Di Ventra, D. N. Basov, *Science* **2009**, *325*, 1518.
- [12] Q. Wang, E. T. F. Rogers, B. Gholipour, C.-M. Wang, G. Yuan, J. Teng, N. I. Zheludev, *Nat. Photonics* **2016**, *10*, 60.
- [13] N. I. Zheludev, E. Plum, *Nat. Nanotechnol.* **2016**, *11*, 16.
- [14] M. Manjappa, Y. K. Srivastava, L. Cong, I. Al-Naib, R. Singh, *Adv. Mater.* **2017**, *29*, 1603355.
- [15] Z. Miao, Q. Wu, X. Li, Q. He, K. Ding, Z. An, Y. Zhang, L. Zhou, *Phys. Rev. X* **2015**, *5*, 041027.
- [16] W. M. Zhu, A. Q. Liu, X. M. Zhang, D. P. Tsai, T. Bourouina, J. H. Teng, X. H. Zhang, H. C. Guo, H. Tanoto, T. Mei, G. Q. Lo, D. L. Kwong, *Adv. Mater.* **2011**, *23*, 1792.
- [17] T. Kan, A. Isozaki, N. Kanda, N. Nemoto, K. Konishi, H. Takahashi, M. Kuwata-Gonokami, K. Matsumoto, I. Shimoyama, *Nat. Commun.* **2015**, *6*, 8422.
- [18] W. M. Zhu, A. Q. Liu, T. Bourouina, D. P. Tsai, J. H. Teng, X. H. Zhang, G. Q. Lo, D. L. Kwong, N. I. Zheludev, *Nat. Commun.* **2012**, *3*, 1274.
- [19] P. Pitchappa, M. Manjappa, C. P. Ho, R. Singh, N. Singh, C. Lee, *Adv. Opt. Mater.* **2016**, *4*, 541.
- [20] S. Fan, W. Suh, J. D. Joannopoulos, *J. Opt. Soc. Am. A* **2003**, *20*, 569.
- [21] H. A. Haus, *Waves and Fields in Optoelectronics*, Prentice Hall, Incorporated, New Jersey, USA, **1984**.
- [22] N. Landy, S. Sajuyigbe, J. Mock, D. Smith, W. Padilla, *Phys. Rev. Lett.* **2008**, *100*, 207402.
- [23] N. Yu, P. Genevet, M. A. Kats, F. Aieta, J. P. Tetienne, F. Capasso, Z. Gaburro, *Science* **2011**, *334*, 333.
- [24] L. Cong, P. Pitchappa, Y. Wu, L. Ke, C. Lee, N. Singh, H. Yang, R. Singh, *Adv. Opt. Mater.* **2017**, *5*, 1600716.
- [25] A. Arbabi, Y. Horie, M. Bagheri, A. Faraon, *Nat. Nano* **2015**, *10*, 937.
- [26] M. Khorasaninejad, W. T. Chen, R. C. Devlin, J. Oh, A. Y. Zhu, F. Capasso, *Science* **2016**, *352*, 1190.
- [27] X. Ni, A. V. Kildishev, V. M. Shalae, *Nat. Commun.* **2013**, *4*, 2807.
- [28] G. Zheng, H. Mühlenbernd, M. Kenney, G. Li, T. Zentgraf, S. Zhang, *Nat. Nano* **2015**, *10*, 308.
- [29] L.-H. Gao, Q. Cheng, J. Yang, S.-J. Ma, J. Zhao, S. Liu, H.-B. Chen, Q. He, W.-X. Jiang, H.-F. Ma, Q.-Y. Wen, L.-J. Liang, B.-B. Jin, W.-W. Liu, L. Zhou, J.-Q. Yao, P.-H. Wu, T.-J. Cui, *Light: Sci. Appl.* **2015**, *4*, e324.

- [30] T. J. Cui, M. Q. Qi, X. Wan, J. Zhao, Q. Cheng, *Light: Sci. Appl.* **2014**, *3*, e218.
- [31] S. Liu, T. J. Cui, Q. Xu, D. Bao, L. Du, X. Wan, W. X. Tang, C. Ouyang, X. Y. Zhou, H. Yuan, H. F. Ma, W. X. Jiang, J. Han, W. Zhang, Q. Cheng, *Light: Sci. Appl.* **2016**, *5*, e16076.
- [32] R. Singh, W. Cao, I. Al-Naib, L. Cong, W. Withayachumnankul, W. Zhang, *Appl. Phys. Lett.* **2014**, *105*, 171101.
- [33] L. Cong, S. Tan, R. Yahiaoui, F. Yan, W. Zhang, R. Singh, *Appl. Phys. Lett.* **2015**, *106*, 031107.
- [34] C. Qu, S. Ma, J. Hao, M. Qiu, X. Li, S. Xiao, Z. Miao, N. Dai, Q. He, S. Sun, *Phys. Rev. Lett.* **2015**, *115*, 235503.
- [35] F. J. Garcia-Vidal, L. Martín-Moreno, J. B. Pendry, *J. Opt. A: Pure Appl. Opt.* **2005**, *7*, S97.
- [36] P. Pitchappa, H. Chong Pei, L. Dhakar, Q. You, N. Singh, L. Chengkuo, *J. Microelectromech. Syst.* **2015**, *24*, 525.
- [37] J. D. Baena, J. Bonache, F. Martin, R. M. Sillero, F. Falcone, T. Lopetegi, M. A. Laso, J. Garcia-Garcia, I. Gil, M. F. Portillo, *IEEE Trans. Microwave Theory Tech.* **2005**, *53*, 1451.